J. Fluid Mech. (2008), *vol.* 603, *pp.* 189–206. © 2008 Cambridge University Press
doi:10.1017/S0022112008000943 Printed in the United Kingdom

Instabilities of plane Poiseuille flow with a streamwise system rotation

S. MASUDA, S. FUKUDA AND M. NAGATA

Department of Aeronautics and Astronautics, Graduate School of Engineering,
Kyoto University, Kyoto, 606-8501, Japan

(Received 6 February 2007 and in revised form 5 February 2008)

We analyse the stability of plane Poiseuille flow with a streamwise system rotation. It is found that the instability due to two-dimensional perturbations, which sets in at the well-known critical Reynolds number, $R_c = 5772.2$, for the non-rotating case, is delayed as the rotation is increased from zero, showing a stabilizing effect of rotation. As the rotation is increased further, however, the laminar flow becomes most unstable to perturbations which are three-dimensional. The critical Reynolds number due to three-dimensional perturbations at this higher rotation case is many orders of magnitude less than the corresponding value due to two-dimensional perturbations. We also perform a nonlinear analysis on a bifurcating three-dimensional secondary flow. The secondary flow exhibits a spiral vortex structure propagating in the streamwise direction. It is confirmed that an antisymmetric mean flow in the spanwise direction is generated in the secondary flow.

1. Introduction

It is important to understand the stability of flows under a system rotation for both engineering and geophysical applications. Compared with a large number of investigations on plane Poiseuille flow with a spanwise system rotation (see Wall & Nagata 2006 and the references therein), the same flow with a streamwise system rotation has attracted less attention despite its importance in the geophysical context, such as instabilities of meridional flows across the equator. As far as we know even the linear stability of the laminar flow has not yet been analysed properly. It is only recently that experimental (Recktenwald, Brücker & Schröder 2004) and numerical (Oberlack *et al.* 2006) investigations of turbulent plane Poiseuille flow with a streamwise rotation have been reported. The most striking feature among other turbulent properties reported is the generation of a mean flow in the spanwise direction.

Plane Poiseuille flow with a streamwise system rotation can be regarded as the narrow-gap limit of an annular Poiseuille flow between concentric rotating cylinders. As a special example of so-called spiral Poiseuille flow (Joseph 1976), where the two concentric cylinders rotate independently (Chung & Astill 1977; Hasoon & Martin 1977; Takeuchi & Jankowski 1981; Cotrell & Pearltein 2004, 2006), the linear stability of the rigid-body rotation case with the radius ratio of 0.5 has been studied by Meseguer & Marques (2002) with the result that the critical state is determined by the non-axisymmetric modes. Non-axisymmetric modes in annular Poiseuille flow correspond to three-dimensional modes in our plane geometry.

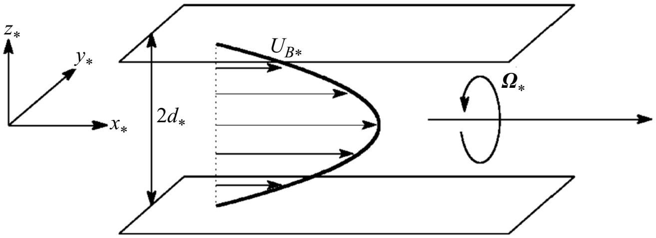

FIGURE 1. The configuration of the model.

We note that the appearance of non-axisymmetric instabilities before the axisymmetric instabilities has also been reported in Hagen–Poiseuille flow with an axial rotation (Pedley 1968, 1969; Cotton & Salwen 1981; Fernandez-Feria & del Pino 2002), although it is difficult to make a direct comparison with the current investigation, because of the differences not only in geometries, but also in the critical states in non-rotational cases (plane and annular Poiseuille flows become unstable at a finite Reynolds number, whereas pipe Poiseuille flow is linearly stable for any finite Reynolds numbers).

The purposes of the current paper are to identify the critical mode for the stability of plane Poiseuille flow with a streamwise rotation and to seek the origin of the spanwise mean flow.

We first describe the results of our linear analysis and then proceed to a nonlinear investigation for the secondary flow which bifurcates as the basic state loses its stability. (We are interested only in the absolute instability, although the appearance of convective instability before absolute instability is a possibility.) We do find a spanwise mean flow in the three-dimensional secondary flow. Results are compared with the direct numerical simulation by Oberlack *et al.* (2006).

2. Formulation

2.1. *Configuration*

We consider a viscous incompressible fluid motion of a fluid with density ρ_* between two parallel plates with a gap width, $2d_*$, induced by a constant pressure gradient under the system rotation Ω_*. The orientation of the system rotation is parallel to the pressure gradient (figure 1). We take the origin of the coordinate system on the midplane between the plates, with the x_*- and y_*-coordinates being in the streamwise and spanwise directions, respectively, and the z_*-coordinate being normal to the plates. Corresponding to the x_*-, y_*- and z_*-coordinates, we define the unit vectors $\boldsymbol{i}$, $\boldsymbol{j}$ and $\boldsymbol{k}$. The basic flow with a quadratic velocity profile, i.e. the plane Poiseuille flow, $U_{B*}(z_*)$, is not affected by the rotation. We are interested in investigating the stability of the basic flow and analysing the nature of a secondary flow which may bifurcate when the basic flow loses its stability.

2.2. *The governing equations and the basic state*

In order to non-dimensionalize the system, we take d_* as the length scale, d_*^2/ν as the time scale, ν/d_* as the velocity scale and $\rho_*\nu^2/d_*^2$ as the pressure scale, where ν is the kinematic viscosity. Then, the equations of continuity and the conservation of momentum are written as

$$\nabla\cdot\boldsymbol{u} = 0 \tag{2.1}$$

and

$$\frac{\partial \boldsymbol{u}}{\partial t} + (\boldsymbol{u}\cdot\nabla)\boldsymbol{u} = -\nabla \Pi + \nabla^2 \boldsymbol{u} - \Omega \boldsymbol{i} \times \boldsymbol{u}, \tag{2.2}$$

where $\boldsymbol{u}$ is the velocity, Π is the pressure and Ω is the rotation number defined by

$$\Omega = \frac{2\Omega_* d_*^2}{\nu}. \tag{2.3}$$

The governing equations are to be solved subject to the no-slip boundary condition on the plates:

$$\boldsymbol{u} = \boldsymbol{0} \qquad \text{at} \qquad z = \pm 1. \tag{2.4}$$

Assuming that the basic flow $\boldsymbol{U}_B$ is unidirectional in the x-direction depending only on the z-coordinate when the imposed pressure gradient $\partial\Pi/\partial x$ is constant, we obtain

$$U_B(z) = \boldsymbol{U}_B \cdot \boldsymbol{i} = R(1 - z^2), \tag{2.5}$$

where we have used the value, $U_{0*} = U_{B*}(0)$, of the basic flow on the midplane $z = 0$ to define the Reynolds number

$$R = \frac{U_{0*} d_*}{\nu}. \tag{2.6}$$

The stability of the basic state as well as the development of a new flow field due to the loss of stability is governed by two non-dimensional parameters, R and Ω.

2.3. *The disturbance equations*

In order to analyse the stability of the basic state and to seek solutions other than the basic state we superimpose disturbances, $\hat{\boldsymbol{u}}$ and $\hat{\Pi}$, on the basic state.

$$\boldsymbol{u} = \boldsymbol{U}_B + \hat{\boldsymbol{u}}, \qquad \Pi = \Pi_B + \hat{\Pi}. \tag{2.7}$$

Substituting (2.7) into (2.1) and (2.2) we find that the disturbances satisfy the following equations.

$$\nabla \cdot \hat{\boldsymbol{u}} = 0, \tag{2.8}$$

$$\frac{\partial \hat{\boldsymbol{u}}}{\partial t} + (\hat{\boldsymbol{u}}\cdot\nabla)(U_B \boldsymbol{i} + \hat{\boldsymbol{u}}) + (U_B \boldsymbol{i}\cdot\nabla)\hat{\boldsymbol{u}} = -\nabla\hat{\Pi} + \nabla^2\hat{\boldsymbol{u}} - \Omega \boldsymbol{i} \times \hat{\boldsymbol{u}}. \tag{2.9}$$

The no-slip boundary condition for $\hat{\boldsymbol{u}}$ is given by

$$\hat{\boldsymbol{u}} = \boldsymbol{0} \qquad \text{at} \qquad z = \pm 1. \tag{2.10}$$

For convenience, the velocity disturbance $\hat{\boldsymbol{u}}$ is separated into the mean parts, $\check{U}(t, z)$ in the streamwise direction and $\check{V}(t, z)$ in the spanwise direction, and the residual $\check{\boldsymbol{u}} = (\check{u}, \check{v}, \check{w})^T$,

$$\hat{\boldsymbol{u}} = \check{U}(t, z)\boldsymbol{i} + \check{V}(t, z)\boldsymbol{j} + \check{\boldsymbol{u}}, \tag{2.11}$$

so that

$$\check{U}(t, z) = \overline{\hat{\boldsymbol{u}}} \cdot \boldsymbol{i}, \quad \check{V}(t, z) = \overline{\hat{\boldsymbol{u}}} \cdot \boldsymbol{j}, \tag{2.12}$$

where the x, y-average is indicated by an overbar. By definition the x, y-average of the residual vanishes:

$$\overline{\check{\boldsymbol{u}}} = 0. \tag{2.13}$$

We anticipate that the mean parts, $\check{U}(t, z)$ and $\check{V}(t, z)$, are created by the Reynolds stress (see (2.21) and (2.22)). It is worthing mentioning that in contrast to Wall & Nagata (2006), where only the mean flow modification in the streamwise direction

$\check{U}(t, z)$ was considered, we incorporate the generation of the mean flow in the spanwise direction $\check{V}(t, z)$ as well. The symmetry pertinent to the current problem is represented by

$$(\check{u}, \check{v}, \check{w})(x, y, z) = (\check{u}, \check{v}, \check{w})\left(x + \frac{\pi}{\alpha}, y + \frac{\pi}{\beta}, z\right), \tag{2.14}$$

$$(\check{u}, \check{v}, \check{w})(x, y, z) = (\check{u}, -\check{v}, -\check{w})\left(x, -y + \frac{\pi}{\beta}, -z\right). \tag{2.15}$$

It can be shown from the spatial symmetry described above (the Reynolds stress terms can be proved to be $\overline{\check{\boldsymbol{u}}\check{\boldsymbol{w}}}(-z) = -\overline{\check{\boldsymbol{u}}\check{\boldsymbol{w}}}(z)$, and $\overline{\check{\boldsymbol{v}}\check{\boldsymbol{w}}}(-z) = \overline{\check{\boldsymbol{u}}\check{\boldsymbol{v}}}(z)$ by (2.15).) that the mean flow in the streamwise direction $\check{U}$ is symmetric in z and the mean flow in the spanwise direction $\check{V}$ is antisymmetric in z.

The residual $\check{\boldsymbol{u}}$, which is solenoidal, is further separated into the poloidal and the toroidal parts as

$$\check{\boldsymbol{u}} = \nabla \times \nabla \times (\phi \boldsymbol{k}) + \nabla \times (\psi \boldsymbol{k}) = (\partial^2_{xz}\phi + \partial_y \psi, \partial^2_{yz}\phi - \partial_x \psi, -\Delta_2 \phi)^T, \tag{2.16}$$

where $\Delta_2 = \partial^2_{xx} + \partial^2_{yy}$, so that the total velocity field is now given by

$$\boldsymbol{u} = \boldsymbol{U}_B(z) + \check{U}(t, z)\boldsymbol{i} + \check{V}(t, z)\boldsymbol{j} + \nabla \times \nabla \times (\phi \boldsymbol{k}) + \nabla \times (\psi \boldsymbol{k}). \tag{2.17}$$

Note that (2.13) requires $\overline{\phi} = \overline{\psi} \equiv 0$. The horizontal symmetry (2.14) and the reflection symmetry (2.15) are imposed on ϕ and ψ later (see (4.10)).

The no-slip boundary condition (2.10) leads to

$$\check{U} = \check{V} = \phi = \frac{\partial \phi}{\partial z} = \psi = 0 \quad \text{at} \quad z = \pm 1. \tag{2.18}$$

After substituting (2.17) into (2.9) we operate $\boldsymbol{k} \cdot (\nabla \times \nabla \times$ and $\boldsymbol{k} \cdot (\nabla \times$ on (2.9) to obtain

$$\partial_t \nabla^2 \Delta_2 \phi + ((U_B + \check{U})\partial_x \nabla^2 + \check{V}\partial_y \nabla^2 - \nabla^4 - (U_B + \check{U})''\partial_x - \check{V}''\partial_y)\Delta_2 \phi \\ + \varOmega \partial_x \Delta_2 \psi + \boldsymbol{\delta}((\check{\boldsymbol{u}} \cdot \nabla)\check{\boldsymbol{u}}) = 0, \tag{2.19}$$

$$\partial_t \Delta_2 \psi + ((U_B + \check{U})\partial_x + \check{V}\partial_y - \nabla^2)\Delta_2 \psi \\ - ((U_B + \check{U})'\partial_y + \varOmega \partial_x - \check{V}'\partial_x)\Delta_2 \phi - \boldsymbol{\epsilon}((\check{\boldsymbol{u}} \cdot \nabla)\check{\boldsymbol{u}}) = 0, \tag{2.20}$$

where the prime, denotes differentiation with respect to z (there should be no confusion in adopting a different usage of primes in § 4.2, where primes are operated on integers to distinguish between odd and even integers). The nonlinear terms, $\boldsymbol{\delta}((\check{\boldsymbol{u}} \cdot \nabla)\check{\boldsymbol{u}}) \equiv \boldsymbol{k} \cdot (\nabla \times \nabla \times ((\check{\boldsymbol{u}} \cdot \nabla)\check{\boldsymbol{u}}))$ and $\boldsymbol{\epsilon}((\check{\boldsymbol{u}} \cdot \nabla)\check{\boldsymbol{u}}) \equiv \boldsymbol{k} \cdot (\nabla \times ((\check{\boldsymbol{u}} \cdot \nabla)\check{\boldsymbol{u}}))$, which appear in (2.19) and (2.20), respectively, are expressed explicitly in the Appendix.

The equations for the mean parts $\check{U}(t, z)$ and $\check{V}(t, z)$ can be obtained by taking the x, y-averages of the x- and y-components, respectively, of (2.9):

$$\check{U}'' - \partial_z \overline{\check{\boldsymbol{u}}\check{\boldsymbol{w}}} \equiv \check{U}'' + \partial_z \overline{\Delta_2 \phi \left(\partial^2_{zx}\phi + \partial_y \psi\right)} = \frac{\partial \check{U}}{\partial t}, \tag{2.21}$$

$$\check{V}'' - \partial_z \overline{\check{\boldsymbol{v}}\check{\boldsymbol{w}}} \equiv \check{V}'' + \partial_z \overline{\Delta_2 \phi \left(\partial^2_{zy}\phi - \partial_x \psi\right)} = \frac{\partial \check{V}}{\partial t}. \tag{2.22}$$

3. The linear analysis

3.1. *The numerical method*

Since the mean parts, $\check{U}(t,z)$ and $\check{V}(t,z)$, are created by the Reynolds stresses, where disturbances interact quadratically (see (2.21) and (2.22)), they do not participate in the linear analysis. Omitting $\check{U}(t,z)$, $\check{V}(t,z)$ and nonlinear terms $\delta((\check{\boldsymbol{u}}\cdot\nabla)\check{\boldsymbol{u}})$ and $\epsilon((\check{\boldsymbol{u}}\cdot\nabla)\check{\boldsymbol{u}})$ in (2.19) and (2.20), we obtain

$$\frac{\partial}{\partial t}\nabla^2\Delta_2\phi = \left(\nabla^4 + U_B''\partial_x - U_B\partial_x\nabla^2\right)\Delta_2\phi - \Omega\partial_x\Delta_2\psi, \tag{3.1}$$

$$\frac{\partial}{\partial t}\Delta_2\psi = \left(U_B'\partial_y + \Omega\partial_x\right)\Delta_2\phi + (\nabla^2 - U_B\partial_x)\Delta_2\psi. \tag{3.2}$$

We note that when $\Omega = 0$, i.e. in the case of non-rotating plane Poiseuille flow, (3.1) is independent of the toroidal component ψ, and the solutions to (3.1) and (3.2) are classified into two classes of eigenmodes. Members of the first class of eigenmodes, where ϕ is determined by (3.1) and ψ is found by solving (3.2) which is inhomogeneous with non-vanishing $U_B'\partial_y\Delta_2\phi$, are called the Orr–Sommerfeld mode (O-S mode). Members of the second class of eigenmodes, where $\phi \equiv 0$ and ψ satisfies homogeneous (3.2), are called the Squire mode (see, for example, Schmid & Henningson 2001). The toroidal component ψ of the O-S mode is absent when Squire's theorem is applied, i.e. $\partial_y \equiv 0$, with the stability being determined solely by the poloidal component ϕ. We extend this classification to the rotational case. When $\Omega \neq 0$, Squire's theorem does not hold, so that the three-dimensional form of perturbations with the streamwise and spanwise wavenumbers, α and β, must be taken into consideration in general.

In order to solve the equations above by the normal mode ansatz we expand ϕ and ψ using the Chebyshev polynomials $T_\ell(z)$ as follows:

$$\phi = \sum_{l=0}^{\infty} a_l(1-z^2)^2 T_\ell(z)\exp(\mathrm{i}\alpha x + \mathrm{i}\beta y + \sigma t), \tag{3.3}$$

$$\psi = \sum_{l=0}^{\infty} b_l(1-z^2) T_\ell(z)\exp(\mathrm{i}\alpha x + \mathrm{i}\beta y + \sigma t), \tag{3.4}$$

where σ is the growth rate and the factors, $(1-z^2)^2$ for ϕ and $(1-z^2)$ for ψ, are incorporated so that the boundary conditions

$$\phi = \frac{\partial\phi}{\partial z} = \psi = 0 \quad \text{at} \quad z = \pm 1 \tag{3.5}$$

are satisfied automatically. For numerical purposes, the infinite series in (3.3) and (3.4) must be truncated by using only the first $(L+1)$ terms.

The evaluation of (3.1) and (3.2) at the collocation points

$$z_i = \cos\left(\frac{\mathrm{i}\pi}{L+2}\right) \qquad (i = 1, \ldots, L+1), \tag{3.6}$$

after (3.3) and (3.4) are substituted, leads us to the eigenvalue problem

$$A_{ij}x_j = \sigma B_{ij}x_j, \; x_j \in (a_l, b_l) \qquad (l = 0, 1, \ldots, L), \tag{3.7}$$

Ω	R	$L=10$	$L=20$	$L=30$
140	0	(−10.703905, −22.644485)	(−10.703907, −22.644491)	(−10.703907, −22.644491)
140	100	(6.100084, −34.495072)	(6.098971, −34.492437)	(6.098971, −34.492437)
140	200	(17.869938, −68.809149)	(17.869569, −68.779014)	(17.869569, −68.779014)
1000	0		(−24.300618, 420.425818)	(−24.300621, −420.425816)
1000	100		(−24.492633, −597.832466)	(−24.492639, −597.832471)
1000	200		(−25.343430, −783.227939)	(−25.343436, −783.227962)

TABLE 1. The eigenvalue σ with $\alpha=0.5$, $\beta=2.5$ for $\Omega=140$ and $\alpha=2.0$, $\beta=4.0$ for $\Omega=1000$ at the truncation level L. The first number in the parentheses is the real part of σ and the second is the imaginary part.

with σ as the eigenvalue. We solve (3.7) numerically by using the package DGVCCG of IMSL software library (Visual Numerics Inc. 1990) which uses the QZ algorithm. Once the eigenvalue σ is determined, the associated eigenfunctions,

$$\Phi(z)=\sum_{l=0}^{L} a_l(1-z^2)^2 T_\ell(z), \tag{3.8}$$

$$\Psi(z)=\sum_{l=0}^{L} b_l(1-z^2) T_\ell(z), \tag{3.9}$$

are calculated.

The eigenvalues σ are compared with regard to the truncation level L for typical cases in table 1. We see that $L=20$ gives an accuracy which is more than sufficient for our purpose. Therefore, we choose $L=20$ in the following calculations unless stated otherwise.

3.2. *Results*

Figure 2 shows the curves of $\mathrm{Re}[\sigma]=0$ in the (Ω, R)-plane for various wavenumber pairs (α, β). We can see from figure 2 that the flow is unstable at a large Reynolds number against two-dimensional perturbations ($\beta=0$) for $\Omega\simeq 0$. We find that two-dimensional perturbations dominate for $\Omega\lesssim 33.923$ and that three-dimensional perturbations become responsible for instability for $\Omega\gtrsim 33.923$. Figure 2 indicates that the critical Reynolds number, R_c, decreases rapidly as Ω increases slightly over 33.923 and that it takes an almost constant value for large Ω. (In fact, $R_c=66.50$ at $\Omega=1000$, 66.46 at $\Omega=2000$ and 66.45 at $\Omega=3000$). When $\Omega>500$, the streamwise wavenumber α of the three-dimensional perturbations corresponding to the critical Reynolds number decreases as Ω increases, while the spanwise wavenumber β remains at an almost constant value, $\beta\approx 2.5$. The existence of two asymptotic regimes for the three-dimensional perturbations, namely, $\Omega\simeq 33.923$ at large R and $R_c\simeq 66.45$ at large Ω, can be compared with those in the rigid-body rotation case of the spiral Poiseuille flow with the radius ratio 0.5 of the two cylinders (Meseguer & Marques 2002) where the two regimes are determined by the non-axisymmetric modes with the azimuthal wavenumber $n=5$ and $n=6$.

3.2.1. *Two-dimensional perturbations*

We choose $L=50$ to calculate the critical Reynolds number for two-dimensional perturbations which take place at a larger R region. The envelope curve which originates on the R-axis in figure 2 corresponds to the neutral curve due to the O-S mode with $\alpha=1.02$ and $\beta=0$ at $\Omega=0$. As Ω departs from zero, the critical

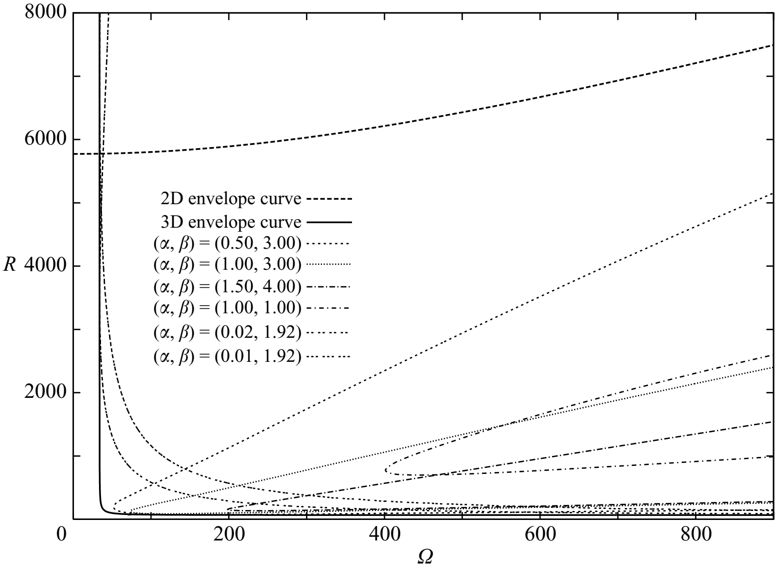

FIGURE 2. The neutral curves in the (Ω, R)-plane for various wavenumber pairs. α varies along the two-dimensional envelope curve with $\beta = 0$, while both α and β vary along the three-dimensional envelope curve. The two-dimensional envelope curve intersects the R-axis at $R = 5772.2$ with $\alpha = 1.02$. The three-dimensional envelope curve seems to have asymptotes at large R and at large Ω.

Reynolds number increases gradually from the well-known value, 5772.2, for the non-rotational case, showing the stabilizing effect of rotation. The corresponding critical wavenumber α_c decreases only slightly with increasing Ω along this envelope (for example $\alpha_c = 1.014$ at $\Omega = 500$).

The eigenvalues,

$$\sigma = -\mathrm{i}\alpha c, \tag{3.10}$$

where c is the phase speed, at $R = 10\,000$ and $\Omega = 140$ with $\alpha = 1.0$ and $\beta = 0$ are plotted in the complex plane $(c_r, c_i) \equiv (\mathrm{Re}[c], \mathrm{Im}[c])$ in figure 3. Eigenvalues corresponding to both O-S modes and Squire modes are shown. To avoid confusion, only eigenvalues corresponding to antisymmetric (even streamfunction) O-S modes are shown; those corresponding to the symmetric (odd streamfunction) perturbations calculated first by Orszag (1971) are not included. (The black square at the top right-hand corner in figure 3 will be explained later.) It is confirmed that the distribution of the eigenvalues of the O-S modes at $\Omega = 140$ in the figure hardly change from that with $\Omega = 0$: there are three distinct families, A-family, S-family and P-family (Mack 1976). As we can see, the distribution of the eigenvalues of the Squire modes in the complex plane follows the same pattern as the O-S modes. We can also see in figure 3 that there is only one eigenvalue with $\mathrm{Re}[\sigma] \equiv \alpha \mathrm{Im}[c] > 0$ and it belongs to the A-family of the O-S modes. The eigenfunctions, $\Phi(z)$ and $\Psi(z)$, corresponding to this eigenvalue, but at $R = 5772.3$ and $(\alpha, \beta) = (1.02, 0)$, are depicted in figure 4. The eigenfunction $\Phi(z)$, with suitable multiplication by a constant, could be regarded as the streamfunction which is often adopted in the conventional two-dimensional analysis because the perturbation velocity due to the poloidal component ϕ in the two-dimensional case is given by $(\mathrm{i}\alpha\Phi_z, 0, -\alpha^2\Phi)^T$ and, therefore, $\mathrm{i}\alpha\Phi$ represents the streamfunction in the (x, z) plane. It can be seen that there are hardly any effects

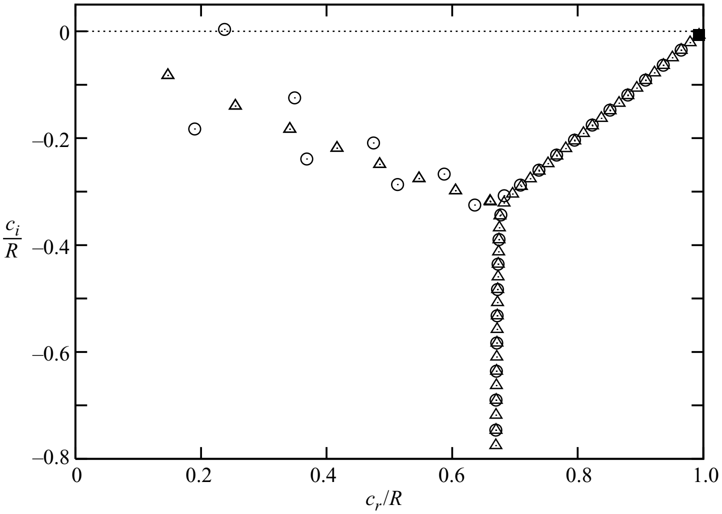

FIGURE 3. The distribution of the eigenvalues in the complex plane at $R = 10\,000$, $\Omega = 140$, with $(\alpha, \beta) = (1.0, 0)$. Circles, the O-S modes; triangles, the Squire modes. The eigenvalue with the largest real part on the α-axis in Figure 5 is traced back to the eigenvalue at the top right-hand corner in this figure indicated by the black square.

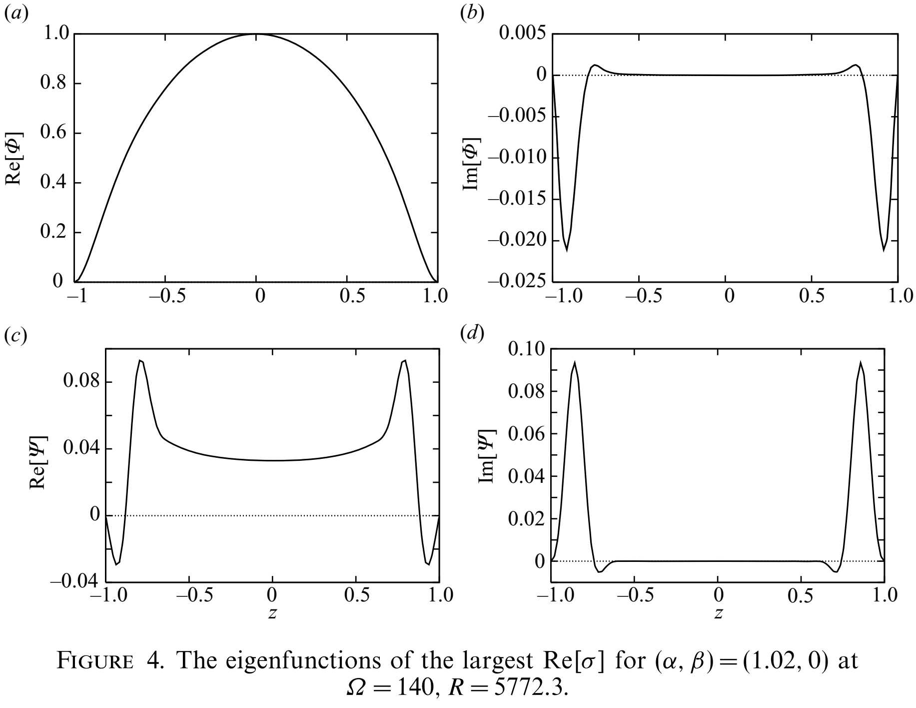

FIGURE 4. The eigenfunctions of the largest $\mathrm{Re}[\sigma]$ for $(\alpha, \beta) = (1.02, 0)$ at $\Omega = 140$, $R = 5772.3$.

of rotation on the eigenfunction $\Phi(z)$ when our figures 4(*a*) and 4(*b*) at $\Omega = 140$ are compared with those in the two-dimensional analysis for $\Omega = 0$ described in, for instance, Drazin & Reid (1978): the eigenfunction $\Phi(z)$ is characterized typically by a Gaussian-like distribution for its real part (figure 4(*a*)) and a small but sharp concentrated distribution near both walls for its imaginary part (figure 4*b*). The

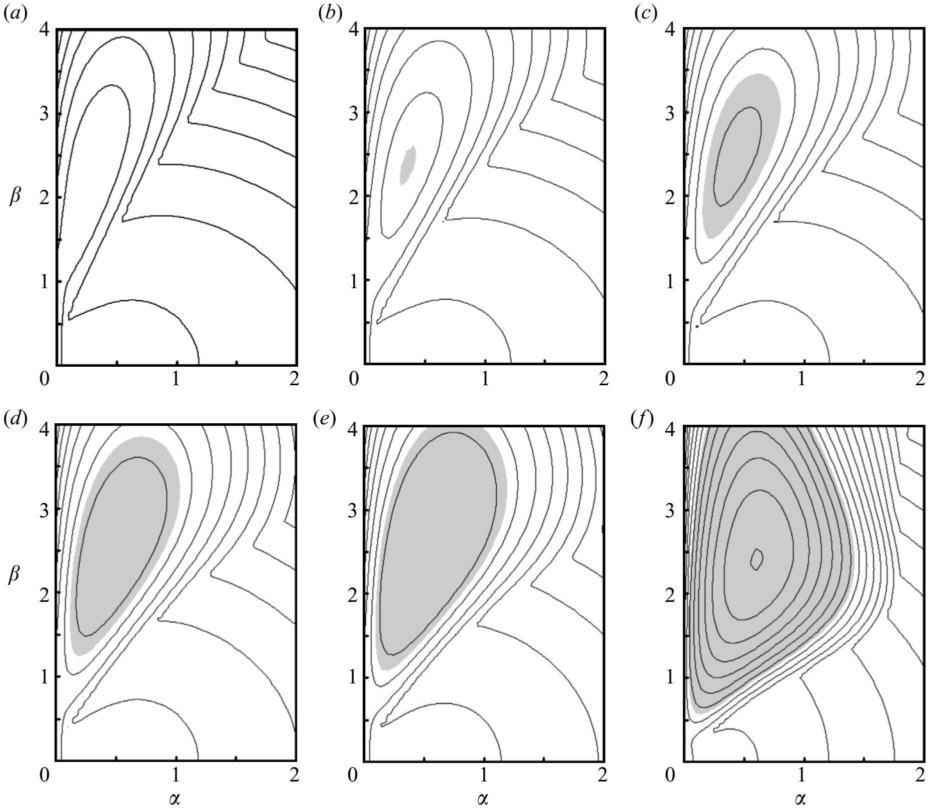

FIGURE 5. The unstable region indicated by a dark area in the (α, β) plane for $\Omega = 140$. (*a*) $R = 60$, (*b*) $R = 70$, (*c*) $R = 80$, (*d*) $R = 90$, (*e*) $R = 100$ and (*f*) $R = 200$.

rotational effect is observed as the generation of the eigenfunction $\Psi(z)$ owing to non-vanishing $\Omega \partial_x \Delta_2 \phi$ in (3.2) which reveals a strong concentration of the spanwise component of the perturbation velocity, $(0, -\mathrm{i}\alpha\Psi, 0)^T$, near the walls as indicated in figures 4(*c*) and (*d*).

3.2.2. *Three-dimensional perturbations*

In order to present an example of the instability due to three-dimensional perturbations that occurs for $\Omega \gtrsim 33.923$, we plot the contours of $\mathrm{Re}[\sigma]$ on the (α, β)-plane for various values of R in figure 5 when $\Omega = 140$. The plane is divided into two regions depending on the dominant eigenvalue: one attached to the α-axis and the other to the β-axis (figure 5*a*). As R is increased, instability emerges in the region attached to the β-axis at around $\beta = 2.3$ with small α (figure 5*b*). As R is further increased, the instability region expands in size but never touches the β-axis (figures 5*c*–*f*)). On the other hand, instabilities never appear in the region attached to the α-axis.

The dominant eigenvalue in each region in the (α, β)-plane is easily identified when the eigenvalues with the first two largest real parts are plotted against α for a fixed β (figure 6). Figure 6(*a*) shows that the real part of the eigenvalue which is the largest at $\alpha = 0$ increases at first and decreases after it reaches its peak at $\alpha \approx 0.3 \sim 0.5$ depending on R, as α is increased. It is found that the peak first reaches $\mathrm{Re}[\sigma] = 0$ when $R = 69.39$ at $(\alpha, \beta) = (0.35, 2.36)$ for $\Omega = 140$. The eigenmode with

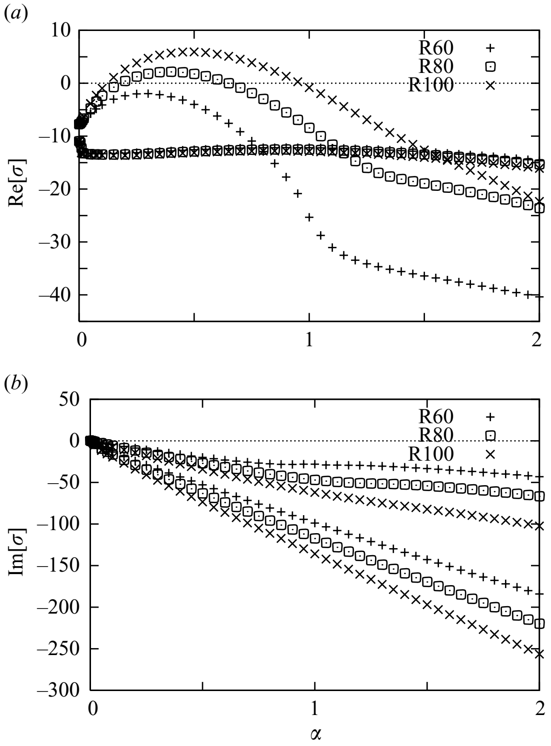

FIGURE 6. The eigenvalues σ corresponding to the two largest real parts for $R = 60$, 80 and 100 with $\beta = 2.3$, $\Omega = 140$. (*a*) the real part, (*b*) the imaginary part. The real parts of the three curves in the upper group in (*b*) correspond to those which are dominant for smaller α in (*a*).

this eigenvalue is the one that is dominant in the region attached to the β-axis. Figure 6 also shows that the eigenvalue which has the second largest real part at $\alpha = 0$ keeps an almost constant negative value for its real part and becomes dominant for larger α. The eigenmode with this eigenvalue is the one that is dominant in the region attached to the α-axis in figure 5. The imaginary parts of both the first and the second eigenvalues decrease monotonically as α is increased.

Now, we analyse the eigenmode which dominates in the region attached to either the α-axis or the β-axis in more detail. As for the eigenmode which dominates in the region attached to the β-axis, the symmetries of ϕ and ψ in z are broken because $\beta \neq 0$ and U_B' in (3.2) is antisymmetric in z. As a result the eigenfunctions, $\Phi(z)$ and $\Psi(z)$, become asymmetric as shown in figure 7 for $R = 69.4$ and $\Omega = 140$ at $(\alpha, \beta) = (0.35, \pm 2.36)$. All the peaks in the figures are seen to be biased towards the wall either at $z = 1$ or $z = -1$ depending on the sign of β. We have traced this eigenvalue carefully back to the parameter values, $R = 10\,000$, $\Omega = 0$ and $(\alpha, \beta) = (1.0, 0)$ and found it originates from the same O-S mode that has caused the two-dimensional instability.

Since the eigenmode which dominates in the region attached to the α-axis in figure 5 is never involved in instabilities, we describe the associated eigefunctions only briefly. The eigenfunctions, $\Phi(z)$ and $\Psi(z)$ for $R = 69.4$ and $\Omega = 140$ at $(\alpha, \beta) = (0.35, 0)$ are shown in figure 8. We see that the peaks of $\mathrm{Re}[\Phi(z)]$ and $\mathrm{Re}[\Psi(z)]$ are centred in the middle. The distributions of $\mathrm{Im}[\Phi(z)]$ and $\mathrm{Im}[\Psi(z)]$ are smoother and their peaks are situated more towards the centre than their counterparts in figure 4. Again, we have traced this eigenvalue back to the parameter values, $R = 10\,000$, $\Omega = 0$ and

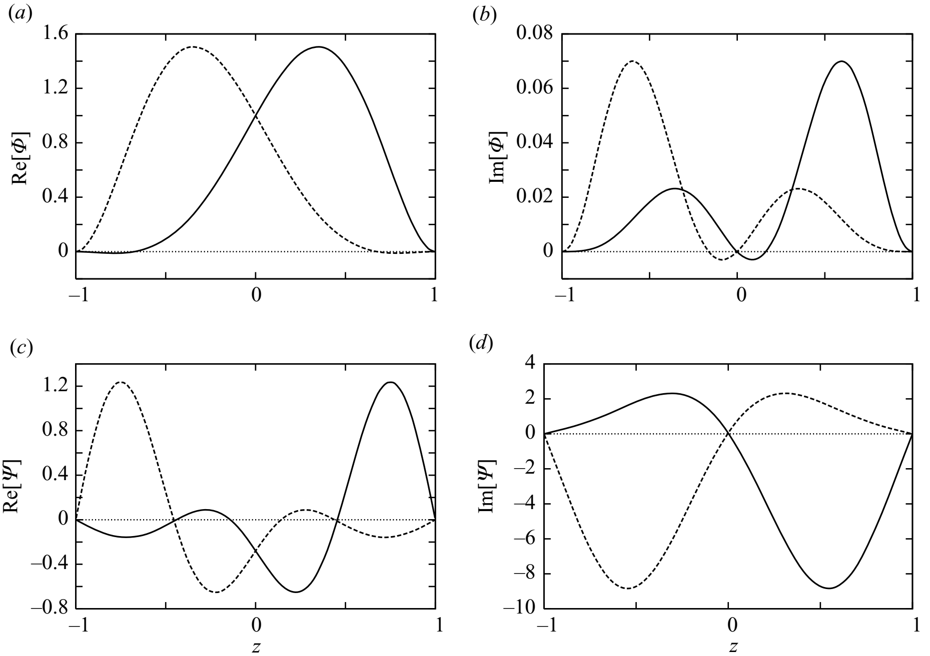

FIGURE 7. The eigenfunctions of the largest Re[σ] at $(\alpha, \beta) = (0.35, 2.36)$: solid curve and at $(\alpha, \beta) = (0.35, -2.36)$: dotted curve. $\Omega = 140$, $R = 69.4$.

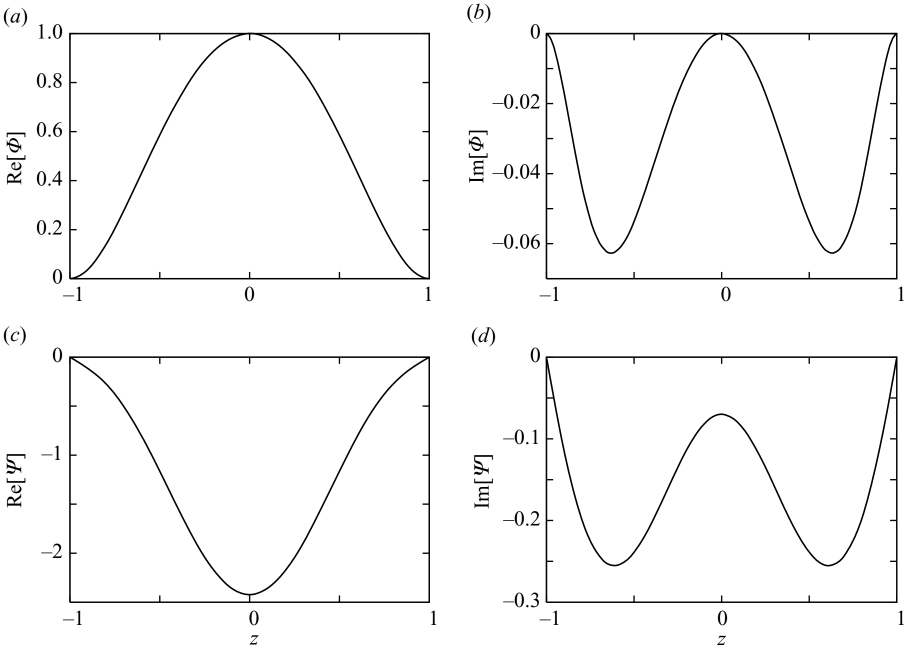

FIGURE 8. The eigenfunctions of the largest Re[σ] for $(\alpha, \beta) = (0.35, 0)$ at $\Omega = 140$, $R = 69.4$.

$(\alpha, \beta) = (1.0, 0)$ and identified its origin as one of the Squire mode indicated by the black square at the top-right corner of figure 3.

Going back to figure 6, we notice that the numerical values of the two eigenvalues at $\alpha = 0$ are the same for all R. Actually, they are $(-7.7540, 0.0)$ and $(-10.9745, 0.0)$. We obtain these values analytically, below. When $\alpha = 0$, (3.1) and (3.2) are simplified as

$$\sigma(\phi'' - \beta^2\phi) = \phi'''' - 2\beta^2\phi'' + \beta^4\phi, \tag{3.11}$$

$$\sigma\psi = -2\beta \mathrm{i} R z\phi + \psi'' - \beta^2\psi. \tag{3.12}$$

Note that (3.11) decouples from (3.12) and that the stability can be determined by solving only (3.11). Since (3.11) does not involve parameters other than β, the eigenvalues at $\alpha = 0$ do not depend on R or Ω. (In fact, the eigenvalues at $\alpha = 0$ are the same for any form of unidirectional flow, irrespective of whether it is subject to streamwise rotation or not.) Together with the boundary condition $\phi(\pm 1) = \phi'(\pm 1) = 0$, (3.11) leads to the solvability condition (the existence of non-trivial ϕ)

$$4(\beta^2 - \gamma^2)^2 \cosh\gamma \sinh\gamma \left(\frac{\tanh\beta}{\tanh\gamma} + \frac{\tanh\gamma}{\tanh\beta} - \frac{\beta}{\gamma} - \frac{\gamma}{\beta}\right) = 0, \tag{3.13}$$

where $\gamma^2 = \sigma + \beta^2$. The condition $\cosh\gamma = 0$ gives $\gamma = \mathrm{i}(1/2 + k\pi)$, $k = 0, 1, 2, 3$ and the condition $\sinh\gamma = 0$ gives $\gamma = \mathrm{i}(k\pi)$, $k = 1, 2, \ldots$. The value, -7.75740 at $\alpha = 0$ with $\beta = 2.3$ in figure 6 corresponds to $\sigma = -\beta^2 - (\pi/2)^2$, while the other value, $\sigma = -10.9745$ satisfies $\tanh\beta/\tanh\gamma + \tanh\gamma/\tanh\beta = \beta/\gamma + \gamma/\beta$.

4. The nonlinear analysis

It is of interest to find a three-dimensional finite-amplitude solution which is expected to bifurcate first as R is increased for $\Omega \gtrsim 33.923$. Finite-amplitude solutions are governed by (2.19), (2.20), (2.21) and (2.22) subject to the boundary conditions (2.18). Since the eigenvalue is a single complex number, i.e. not a complex conjugate, we anticipate that the solution bifurcating from the linear critical state is of travelling-wave type. Therefore, we expand ϕ, ψ, $\check{U}$ and $\check{V}$ as

$$\phi = \sum_{l=0}^{L} \sum_{\substack{m=-M \\ (m,n)\neq(0,0)}}^{M} \sum_{n=-N}^{N} a_{lmn}\, f_l(z) \exp(\mathrm{i}m\alpha(x - ct) + \mathrm{i}n\beta y), \tag{4.1}$$

$$\psi = \sum_{l=0}^{L} \sum_{\substack{m=-M \\ (m,n)\neq(0,0)}}^{M} \sum_{n=-N}^{N} b_{lmn}\, g_l(z) \exp(\mathrm{i}m\alpha(x - ct) + \mathrm{i}n\beta y), \tag{4.2}$$

$$\check{U}(z) = \sum_{l=0}^{L} c_l\, g_l(z), \tag{4.3}$$

$$\check{V}(z) = \sum_{l=0}^{L} d_l\, g_l(z), \tag{4.4}$$

at the truncation level (L, M, N). The boundary conditions (2.18) are satisfied by taking

$$f_l(z) = (1 - z^2)^2\, T_l(z), \tag{4.5}$$

$$g_l(z) = (1 - z^2)\, T_l(z). \tag{4.6}$$

(L, M, N)	c	$\check{V}_\tau$
(19,7,7)	61.74984	2.91666
(17,6,6)	61.74987	2.91698
(15,5,5)	61.75040	2.91606
(13,4,4)	61.74868	2.91913

TABLE 2. The phase speed c and the momentum transport in spanwise direction $\check{V}_\tau$ of the secondary flow at the truncation level (L, M, N). $\alpha = 0.35$, $\beta = 2.36$, $\Omega = 140$, $R = 100$.

We have set (4.3) and (4.4) in such a way that the mean parts, $\check{U}$ and $\check{V}$, do not depend on time for a travelling-wave solution. To justify this, suppose that $\check{w}(= -\Delta_2\phi)$ in (2.21) and (2.22) has a factor $\exp(\mathrm{i}m\alpha(x - ct) + \mathrm{i}n\beta y)$. Then, it interacts with $\check{u}(= \partial^2_{xz} + \partial_y\psi)$ and $\check{v}(= \partial^2_{yz} - \partial_x\psi)$ with a factor $\exp(\mathrm{i}\mu\alpha(x - ct) + \mathrm{i}\nu\beta y)$, only when $m + \mu = 0$ and $n + \nu = 0$, in order for $\overline{\check{w}\check{u}}$ and $\overline{\check{w}\check{v}}$ to have non-zero values. Therefore, the dependence of the Reynolds stress terms, $\check{w}\check{u}$ and $\check{w}\check{v}$, on time vanishes when they are averaged.

4.1. *Numerical method*

Evaluation of (2.19)–(2.22) at the same collocation points (3.6) that are used in the linear analysis after (4.1)–(4.4) are substituted into them leads us to the algebraic equation

$$A_{ij}x_j + B_{ijk}x_jx_k = 0, \qquad x_j \in (a_{lmn}, b_{lmn}, c_l, d_l, c). \tag{4.7}$$

The unknown vector components $a_{lmn}, b_{lmn}, c_l, d_l, c$ are determined by a Newton–Raphson iterative scheme. Although the number of unknowns is increased by one owing to the inclusion of the unknown phase speed c, the number of unknowns and equations can be matched by fixing, for example, the imaginary part of one of the amplitude coefficients a_{lmn} at zero. This means physically that the flow is frozen at some instance (see Wall & Nagata 2006). The deviation of the phase speed from the linear solution can be used as a nonlinear measure of the secondary flow.

The momentum transports in the streamwise and the spanwise directions,

$$\check{U}_\tau = \left.\frac{\partial \check{U}}{\partial z}\right|_{z=1} \tag{4.8}$$

and

$$\check{V}_\tau = \left.\frac{\partial \check{V}}{\partial z}\right|_{z=1}, \tag{4.9}$$

can also be used as nonlinear measures of the secondary flow.

Numerical convergence with respect to truncation level is tabulated for a typical combination of parameters in table 2. We select $(L, M, N) = (15, 5, 5)$ as a sufficiently accurate truncation level in the following calculations.

4.2. *The symmetry*

It can be easily verified that the spatial symmetry (2.14) and (2.15) of the three-dimensional travelling-wave solutions is equivalent to the following symmetry, which

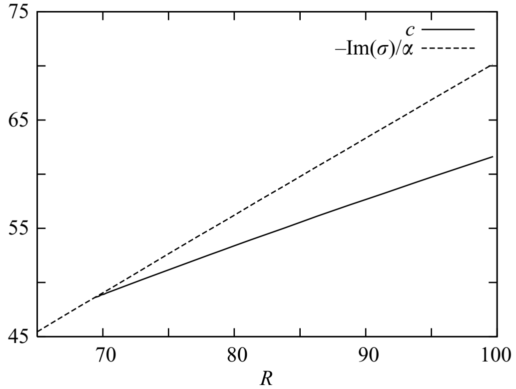

FIGURE 9. The phase speed with $\alpha = 0.35$, $\beta = 2.36$, $\Omega = 140$. The solid curve indicates the nonlinear state whereas the dashed curve corresponds to the linear eigenvalue.

is closed under the nonlinear interactions.

$$\phi, \psi : \left\{ \begin{array}{l} \left\{ \begin{array}{l} \cos m'\alpha(x-ct) \\ \sin m'\alpha(x-ct) \end{array} \right\} \sin n'\beta y \;\; F_{\ell'}(z) \\ \left\{ \begin{array}{l} \cos m'\alpha(x-ct) \\ \sin m'\alpha(x-ct) \end{array} \right\} \cos n'\beta y \;\; F_{\ell''}(z) \\ \left\{ \begin{array}{l} \cos m''\alpha(x-ct) \\ \sin m''\alpha(x-ct) \end{array} \right\} \sin n''\beta y \;\; F_{\ell''}(z) \\ \left\{ \begin{array}{l} \cos m''\alpha(x-ct) \\ \sin m''\alpha(x-ct) \end{array} \right\} \cos n''\beta y \;\; F_{\ell'}(z) \end{array} \right\}. \tag{4.10}$$

The integers m, n and ℓ with a single prime indicate odd integers whereas m, n and ℓ with double primes indicate even integers. The function $F_{\ell'}(z)$ represents the odd function $f_{\ell'}(z)$ or $g_{\ell'}(z)$, whereas $F_{\ell''}(z)$ represents the even function $f_{\ell''}(z)$ or $g_{\ell''}(z)$ (see (4.5) and (4.6)). The above symmetries are imposed in such a way that the amplitude coefficients $a_{\ell mn}$ and $b_{\ell mn}$ for ϕ and ψ which do not belong to the set (4.10) are set to zero initially in the Newton–Raphson iterative scheme. They remain zero throughout successive iterations.

The symmetry described above reveals that the mean flow in the streamwise direction $\check{U}$ is symmetric in z and the mean flow in the spanwise direction $\check{V}$ is antisymmetric in z:

$$\check{U}(-z) = \check{U}(z), \tag{4.11}$$

$$\check{V}(-z) = -\check{V}(z). \tag{4.12}$$

4.3. *Results*

The bifurcation diagram for this system is depicted in figure 9, where the phase speed c of the nonlinear solution is shown to bifurcate at $R = 69.39$ from the curve of $-\mathrm{Re}[\sigma]/\alpha$ for the linear disturbance.

Figure 10 represents the bifurcation nature of the nonlinear solution in terms of the momentum transports $\check{U}_\tau$ and $\check{V}_\tau$. It should be stressed that the momentum transport

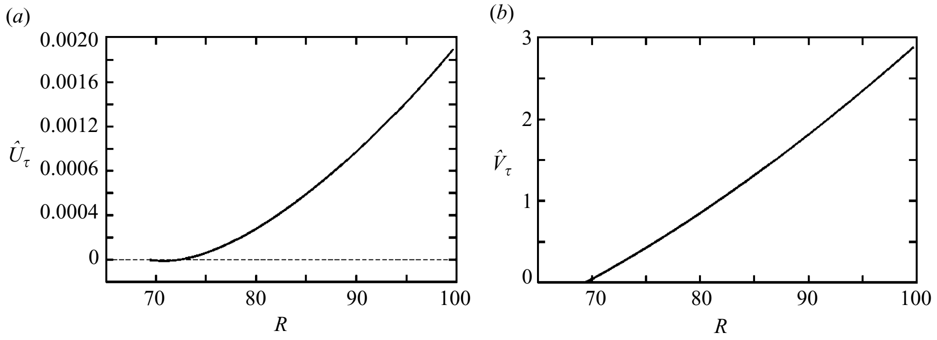

FIGURE 10. The momentum transports. (*a*) $\check{U}_\tau$ in the streamwise direction, (*b*) $\check{V}_\tau$ in the spanwise direction. $\alpha=0.35$, $\beta=2.36$, $\Omega=140$.

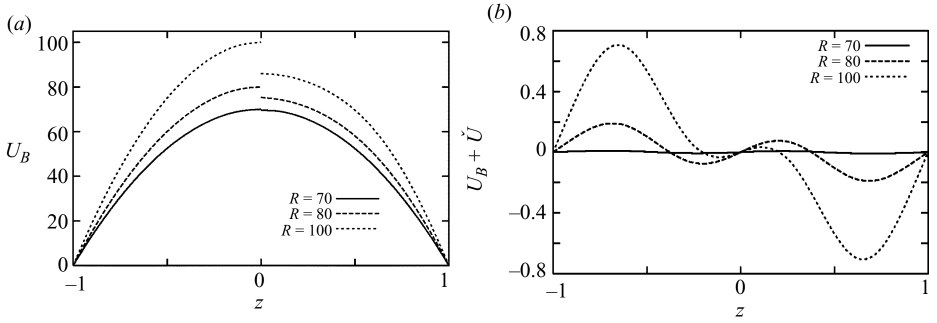

FIGURE 11. (*a*) The total mean flow $U_B+\check{U}$ in the streamwise direction. $-1\leqslant z\leqslant 0$, undisturbed $0\leqslant z\leqslant 1$; disturbed. (*b*) The mean flow $\check{V}$ in the spanwise direction. $R=70, 80, 100$ with $\alpha=0.35$, $\beta=2.36$, $\Omega=140$.

in the spanwise direction, which is absent in the basic laminar state, is generated in the three-dimensional wave travelling in the streamwise direction.

Although the mean flow modification $\check{U}(z)$ itself causes scarcely any changes in the total momentum transport $dU_B/dz|_{z=\pm1}+\check{U}_\tau$ in the streamwise direction, the profile of the total mean flow $U_B+\check{U}$ is changed substantially as is shown in figure 11(*a*) although the modification $\check{U}$ is still not sufficient to produce a inflection point. A part of the energy of the basic flow is transferred to three-dimensional disturbances and is spent partially to generate the mean flow $\check{V}$ in the spanwise direction. The generated mean flow $\check{V}$ in the spanwise direction, the profile of which is antisymmetric in z, amounts to a few per cent of $U_B+\check{U}$ when their peak values are compared even at a Reynolds number about 50 % above its critical value. The vorticity due to $\check{V}$ has the same sign as the background rotation Ω. The peaks of the spanwise mean flow profile in the direct numerical simulation by Oberlack *et al.* (2006) are situated closer to the boundaries $z=\pm1$ than our $\check{V}$ (see their figure 5). These differences probably occur because their Reynolds number $R_{e_\tau}=180$ and the Coriolis parameter $R_o=2.5$, 6.0, 10.0 are extremely large by our corresponding definitions: $R=\frac{1}{2}R_{e_\tau}^2=16\,200$, $\Omega=R_{e_\tau}R_o=450$, 1 080, 1 800. (We abandoned our attempt to continue our solution gradually to their parameter values after we encountered the first turning point of the solution branch at $R=986.2$ for $\Omega=140$. However, this does not exclude the existence of the solution branch at larger parameter values.) Nonetheless, it should be noted that the reverse

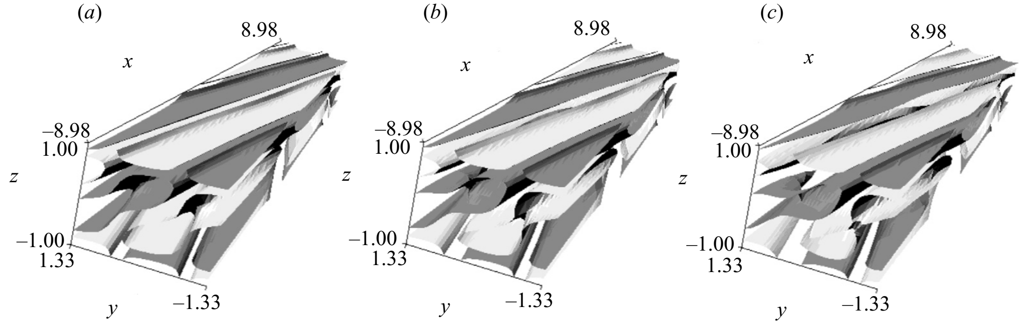

FIGURE 12. The equisurface $\omega = \omega_0$ of the streamwise component of the vorticity of the secondary flow with $\alpha = 0.35$, $\beta = 2.36$, $\Omega = 140$. On the black surfaces $\omega = \omega_0$ and on the grey surfaces $\omega = -\omega_o$. (*a*) $R = 70$, $\omega_0 = 1.70$ ($\omega_{max} = 6.81182$, $\omega_{min} = -6.81277$), (*b*) $R = 80$, $\omega_0 = 8.05$ ($\omega_{max} = 28.6589$, $\omega_{min} = -27.6400$), (*c*) $R = 100$, $\omega_0 = 16.05$ ($\omega_{max} = 49.6988$, $\omega_{min} = -45.9090$).

flow nature of $\check{V}$ adjacent to the midplane $z = 0$ with three inflection points across the channel can also been seen in their direct numerical simulation results. The inflectional flow in the spanwise direction may lead to instabilities of the secondary flow and further bifurcations may ensue.

The flow field of the nonlinear travelling-wave solution throughout the channel is depicted in terms of the streamwise component of the vorticity, $\omega = \boldsymbol{i} \cdot \nabla \times \boldsymbol{u}$, in figure 12. It can be seen that the vortex tubes are twisted more strongly as R is increased.

The twisted nature of the streamwise vorticity is also observed in figure 13, where the cross-sectional disturbed flow components (v, w) are projected onto the (y, z)-plane for one period at the sequential cross-sections $x_n = n\pi/5\alpha$, $(n = -5, -4, \ldots, 3, 4)$. In the first half of the period, the counter-rotating inclined vortices are squeezed near the centreline $z = 0$ to form a double vortex layer with velocity vectors following a figure of eight (figure 13*b*). Then, the knot of the figure eight is loosened (figure 13*c*) and the double vortex layer returns to the single layer again with the vortices standing up straight (figure 13*d*). The vortices are inclined in the same direction as when the sequence started, but the velocity vectors point in the opposite direction (figure 13*f*). In the latter half of the period, the sequence is repeated with the velocity vectors reversed (figures 13*g*–*j*).

5. Concluding remarks

We have analysed the stability of plane Poiseuille flow subject to the streamwise system rotation. It is found that when rotation is added, the instability due to two-dimensional perturbations is delayed. A further increase of rotation leads to three-dimensional instability whose critical Reynolds number is far less than the critical Reynolds number for non-rotating Poiseuille flow. We have also analysed the nonlinear aspect of the bifurcating three-dimensional secondary flow. The secondary flow exhibits a spiral vortex structure propagating in the streamwise direction with a spanwise antisymmetric mean flow.

Investigation of the stability of the secondary flow is underway and detailed results will be reported separately in the near future. A preliminary analysis indicates that the secondary state can be stable for Reynolds numbers slightly above the critical value.

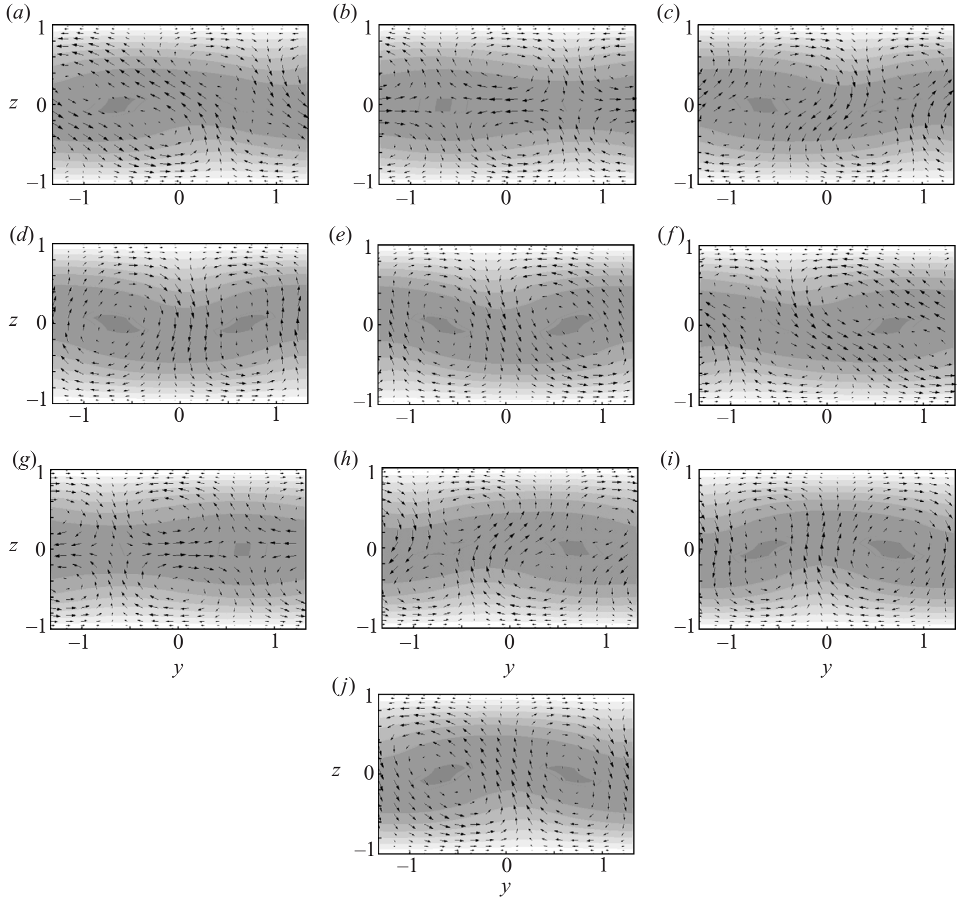

FIGURE 13. The total velocity field of the secondary flow $\boldsymbol{u} = \boldsymbol{U}_B + \check{U}\boldsymbol{i} + \check{V}\boldsymbol{j} + \check{\boldsymbol{u}}$ on the (y, z)-plane with $\alpha = 0.35$, $\beta = 2.36$, $R = 70$, $\Omega = 140$ at $x_n = n\pi/5\alpha$. (*a*) $n = -5$, (*b*) $-4, \ldots,$ (*i*) 3, (*j*) 4. Arrows indicate $(\check{V} + \check{v}, \check{w})$. Darker area indicates stronger streamwise velocity $U_B + \check{U} + \check{u}$.

Appendix. Nonlinear terms $\boldsymbol{\delta}((\check{\boldsymbol{u}} \cdot \nabla)\check{\boldsymbol{u}})$ and $\boldsymbol{\epsilon}((\check{\boldsymbol{u}} \cdot \nabla)\check{\boldsymbol{u}})$

The nonlinear terms $\boldsymbol{\delta}((\check{\boldsymbol{u}} \cdot \nabla)\check{\boldsymbol{u}})$ and $\boldsymbol{\epsilon}((\check{\boldsymbol{u}} \cdot \nabla)\check{\boldsymbol{u}})$, which appear in (2.19) and (2.20), respectively, are expressed explicitly. The differential operators with a prime operate on ϕ or ψ with a prime on the same line. Similarly, the differential operators without a prime operate on ϕ or ψ without a prime on the line.

$$
\begin{aligned}
\boldsymbol{\delta}(\check{\boldsymbol{u}} \cdot \nabla \check{\boldsymbol{u}})) = {} & ((\partial_x \acute{\partial}_x + \partial_y \acute{\partial}_y)(2(\partial_x \acute{\partial}_x + \partial_y \acute{\partial}_y) + \acute{\Delta}_2) - \Delta_2 \acute{\Delta}_2\Big) \phi_z \acute{\phi}_{zz} \\
& + ((\partial_x + \acute{\partial}_x)^2 + (\partial_y + \acute{\partial}_y)^2)\Delta_2((\partial_x \acute{\partial}_x + \partial_y \acute{\partial}_y) - \acute{\Delta}_2)\phi \acute{\phi}_z \\
& - \Delta_2((\partial_x \acute{\partial}_x + \partial_y \acute{\partial}_y) + \acute{\Delta}_2\Big)\phi \acute{\phi}_{zzz} \\
& + (\partial_x \acute{\partial}_y - \partial_y \acute{\partial}_x)(2(\partial_x \acute{\partial}_x + \partial_y \acute{\partial}_y) + \Delta_2)\phi_{zz} \acute{\psi} \\
& + 2(\partial_x \acute{\partial}_y - \partial_y \acute{\partial}_x)(\partial_x \acute{\partial}_x + \partial_y \acute{\partial}_y)\phi_z \acute{\psi}_z \\
& + ((\partial_x + \acute{\partial}_x)^2 + (\partial_y + \acute{\partial}_y)^2)\Delta_2(\partial_x \acute{\partial}_y - \partial_y \acute{\partial}_x)\phi \acute{\psi} \\
& - \Delta_2(\partial_x \acute{\partial}_y - \partial_y \acute{\partial}_x)\phi \acute{\psi}_{zz} \\
& - 2(\partial_x \acute{\partial}_y - \partial_y \acute{\partial}_x)^2 \psi \acute{\psi}_z
\end{aligned}
\qquad \text{(A 1)}
$$

$$\begin{aligned}\boldsymbol{\epsilon}(\check{\boldsymbol{u}}\cdot\nabla\check{\boldsymbol{u}})) = &-\Delta_2\big(\partial_x\acute{\partial}_y-\partial_y\acute{\partial}_x)\phi\acute{\phi}_{zz}\\ &-\acute{\Delta}_2\big(\partial_x(\partial_x+\acute{\partial}_x)+\partial_y(\partial_y+\acute{\partial}_y)\big)\phi_z\acute{\psi}\\ &+\Delta_2(\acute{\partial}_x(\partial_x+\acute{\partial}_x)+\acute{\partial}_y(\partial_y+\acute{\partial}_y))\phi\acute{\psi}_z\\ &-\Delta_2\big(\partial_x\acute{\partial}_y-\partial_y\acute{\partial}_x\big)\psi\acute{\psi}. \qquad \text{(A 2)}\end{aligned}$$

REFERENCES

Drazin, P. G. & Reid, W. H. 1981 *Hydrodynamic Stability*. Cambridge University Press.

Chung, K. C. & Astill, K. N. 1977 Hydrodynamioc instability of viscous flow between rotating coaxial cylinders with fully developed axial flow. *J. Fluid Mech.* **81**, 641–655.

Cotrel, D. L. & Pearlstein, A. J. 2004 The connection between centrifugal instability and Tollmien–Schlichting-like instability for spiral Poiseuille flow. *J. Fluid Mech.* **509**, 331–351.

Cotrel, D. L. & Pearlstein, A. J. 2006 Linear stability of spiral and annular Poiseuille flow for small radius ratio. *J. Fluid Mech.* **547**, 1–20.

Cotton, F. W. & Salwen, H. 1981 Linear stability of rotating Hagen–Poiseuille flow. *J. Fluid Mech.* **108**, 101–125.

Fernandez-Feria, R. & del Pino, C. 2002 The onset of absolute instability of rotating Hagen–Poiseuille flow: a spatial stability analysis. *Phys. Fluids* **14**(9), 3087–3097.

Hasoon, M. A. & Martin, B. W. 1977 The stability of viscous axial flow in an annulus with a rotating inner cylinder. *Proc. R. Soc. Lond.* A**352**, 351–380.

IMSL, Visual Numeric 1990 IMSL/Math Library. Digital Visual Fortran Professional Edition V6.0A, Digital Equipment Corporation Japan.

Joseph, D. D. 1976 *Stability of Fluid Motions*, vols. I and II. Springer.

Mack, L. M. 1976 A numerical study of the temporal eigenvalue spectrum of the Blasius boundary layer. *J. Fluid Mech.* **73**, 497–520.

Meseguer, A. & Marques, F. 2002 On the competition between centrifugal and shear instability in spiral Poiseuille flow. *J. Fluid Mech.* **455**, 129–148.

Oberlack, M., Cabot, W., Pettersson Reif, B. A. & Weller, T. 2006 Group analysis, direct numerical simulation and modelling of a turbulent channel flow with streamwise rotation. *J. Fluid Mech.* **562**, 383–403.

Orszag, S. A. 1971 Accurate solution of the Orr–Sommerfeld stability equation. *J. Fluid Mech.* **50**, 689–703.

Pedley, T. J. 1968 On the instability of rapidly rotating shear flows to non-axisymmetric disturbances. *J. Fluid Mech.* **31**, 603–607.

Pedley, T. J. 1969 On the instability of viscous flow in a rapidly rotating pipe. *J. Fluid Mech.* **35**, 97–115.

Recktenwald, I., Brücker, Ch. & Schröder, W. 2004 PIV investigation of a turbulent channel flow rotating about the streamwise axis. *Adv Turbulence* **10**, 561–564.

Schmid, P. J. & Henningson, D. S. 2001 *Stability and Transition in shear flows.* Applied Mathematical Sciences 142, Springer.

Takeuchi, D. I. & Jankowski, D. F. 1981 A numerical and experimental investigation of the stability of spiral Poiseuille flow. *J. Fluid Mech.* **102**, 101–126.

Wall, D. P. & Nagata, M. 2006 Nonlinear secondary flow through a rotating channel. *J. Fluid Mech.* **564**, 25–55.